

See discussions, stats, and author profiles for this publication at: <https://www.researchgate.net/publication/231651594>

# Silver Particle Nucleation and Growth at Liquid/Liquid Interfaces: A Scanning Electrochemical Microscopy Approach

ARTICLE *in* THE JOURNAL OF PHYSICAL CHEMISTRY C · FEBRUARY 2009

Impact Factor: 4.77 · DOI: 10.1021/jp809165t

---

CITATIONS

13

---

READS

7

4 AUTHORS, INCLUDING:



Martin Andrew Edwards

University of Utah

38 PUBLICATIONS 520 CITATIONS

SEE PROFILE

# Silver Particle Nucleation and Growth at Liquid/Liquid Interfaces: A Scanning Electrochemical Microscopy Approach

Fei Li,<sup>†,‡</sup> Martin Edwards,<sup>†,‡,§</sup> Jidong Guo,<sup>†,||</sup> and Patrick R. Unwin<sup>\*,†</sup>

Department of Chemistry and MOAC Doctoral Training Centre, University of Warwick, Coventry CV4 7AL, United Kingdom

Received: October 16, 2008; Revised Manuscript Received: December 24, 2008

Scanning electrochemical microscopy (SECM) has been used to induce and monitor the electrodeposition of silver particles at a liquid/liquid interface by the electron transfer reaction between aqueous  $\text{Ag}^+$  ions, generated by anodic dissolution of an Ag disk ultramicroelectrode (UME), and bis(pentamethylcyclopentadienyl) iron (decamethylferrocene, DMFc) in a 1,2-dichloroethane (DCE) phase. A two-electrode system with an Ag UME as the SECM tip was used to investigate the factors affecting the deposition process, such as the tip–interface separation, potential applied to the tip, concentration of the reductant in the DCE phase, and the reaction driving force, which was controlled by the concentration ratio of a common ion ( $\text{ClO}_4^-$ ) in the two phases. A theoretical model was developed and rate constants for Ag particle nucleation and growth at the water/DCE interface were obtained by thorough analysis of experimental current–time curves. It was found that  $\text{Ag}^+$  ion adsorption at the interface, coupled to particle nucleation and growth, best described the experimental data. The growth of Ag particles at the liquid/liquid interface was confirmed by independent microscopy measurements.

## 1. Introduction

The unique properties of liquid/liquid (L/L) interfaces, such as freedom from defect sites and the fact that the interfacial potential can be altered, make them an interesting environment for metal deposition via assembly of preformed particles or interfacial growth.<sup>1–14</sup> The basic processes of nucleation and growth at L/L interfaces are similar to those of solid electrodes, i.e., formation of a nucleus, which grows after reaching a critical size<sup>15</sup> to form a particle,<sup>5–9</sup> film,<sup>11,14</sup> or cluster.<sup>12</sup> However, for metal nucleation at L/L interfaces, the metal ion precursor and reducing agent are located in different liquid phases, and the interaction energy between the metal phase formed and the interface is smaller than that at solid electrode substrates. In essence, metal deposition at L/L interfaces may be considered as a useful intermediate case between solution phase metal reduction (relevant to many preparation methods for metallic particles) and conventional electrodeposition.<sup>5</sup> There are wide-ranging applications of metal particles in various areas, such as electrochemistry,<sup>16</sup> homogeneous and supported catalysis,<sup>17</sup> solid-phase synthesis,<sup>18</sup> bioanalysis,<sup>19</sup> and materials science.<sup>20</sup> The electrodeposition of metal particles at L/L interfaces represents an alternative method to traditional chemical and electrochemical methods for preparing and immobilizing metal particles.<sup>8</sup>

Initial research on the formation of metals at L/L interfaces can be traced back to the 19th century, when Faraday formed colloidal gold particles at a L/L interface using a carbon disulfide solution of phosphorus to reduce aqueous solutions of  $\text{AuCl}_4^-$ .<sup>21</sup> This method of spontaneous reduction of gold at L/L interfaces remains an active area of research. For example, Rao et al. have

reported the interfacial reduction of gold at the water/toluene interface and extended the method to the deposition of gold, silver, and copper films.<sup>11</sup> Earlier, the formation of “liquid-like” films of silver by reduction of aqueous silver nitrate solutions in the presence of certain surfactants was described by Efrima and co-workers.<sup>12</sup>

The demonstration of metal deposition at an externally polarized L/L interface was reported by Guainazzi et al. in 1975.<sup>22</sup> In this work, a copper layer was deposited at a water/1,2-dichloroethane (DCE) interface by applying a direct current across the interface between aqueous  $\text{Cu}^{2+}$  and organic  $\text{V}(\text{CO})_6^-$ . Subsequently, Cheng and Schiffrin used an applied potential to control the rate of gold nanoparticle formation at an electrified L/L interface, due to reduction of organic phase  $\text{AuCl}_4^-$  by aqueous  $\text{Fe}(\text{CN})_6^{4-}$ .<sup>3</sup> Polarization measurements at electrified L/L interfaces have been employed to investigate the deposition of a wide range of metal particles on macroscopic and membrane-supported L/L interfaces.<sup>5,6,8–10</sup> To minimize the extent of nucleation at the interface, Guo et al. studied the deposition of individual silver particles at polarized micro- and nano-L/L interfaces, which were supported at the end of tapered glass pipettes.<sup>7</sup>

Scanning electrochemical microscopy (SECM)<sup>23</sup> has become a versatile tool for performing electrochemistry in confined regions and facilitating electrochemical measurements at high spatial resolution.<sup>24,25</sup> SECM has been used for the modification of solid surfaces, such as metal deposition and metal semiconductor etching.<sup>26</sup> Of particular relevance to the studies herein, Mandler et al. employed a micropipette as an SECM tip to form micrometer-sized Ag deposits at a gold substrate by a potential-assisted ion transfer across a L/L interface.<sup>27</sup> Later, this method was developed by combining SECM with nonoptical shear-force detection to significantly increase the lateral resolution of Ag micropatterning.<sup>28</sup> A similar approach has also been used to study metal deposition at carbon nanotube-patterned surfaces.<sup>29</sup>

\* Corresponding author. Phone: +44 (0) 2476 523264. Fax: +44 (0) 2476 524112. E-mail: p.r.unwin@warwick.ac.uk.

<sup>†</sup> Department of Chemistry.

<sup>‡</sup> These authors contributed equally to this work.

<sup>§</sup> MOAC Doctoral Training Centre.

<sup>||</sup> Present address: Department of Biomedical Engineering, University of Memphis, Memphis, TN 38152.

By comparison, the use of SECM to form nanostructures at L/L interfaces is rather limited.

Although metal particle formation at L/L interfaces has been studied for many years, the mechanism and dynamics of particle formation at the interface is still unclear. In this work, SECM was employed to induce the electrodeposition of Ag particles by the electron transfer reaction between aqueous  $\text{Ag}^+$  ions, generated by anodic dissolution of an Ag SECM tip<sup>30,31</sup> and decamethylferrocene (DMFc) in DCE at a nonpolarizable L/L interface. Factors affecting the deposition process, such as the tip–interface separation, the applied potential at the SECM tip, the concentration of the reductant in the DCE phase, and the reaction driving force, which was controlled by the concentration ratio of a common ion ( $\text{ClO}_4^-$ ) in the two phases, were investigated by SECM potential-step chronoamperometry (electrogeneration of  $\text{Ag}^+$  ions). A theoretical model was developed to simulate the experimental current–time curves to obtain quantitative information on the deposition process. Proof of Ag electrodeposition was further obtained through confocal microscopy visualization of the L/L interface.

## 2. Experimental Section

**2.1. Chemicals.** DMFc (Sigma-Aldrich, 97%), silver nitrate ( $\text{AgNO}_3$ , Sigma-Aldrich,  $\geq 99\%$ ), lithium perchlorate ( $\text{LiClO}_4$ , Aldrich, 95+%), tetrabutylammonium perchlorate ( $\text{TBAClO}_4$ , Fluka,  $\geq 99\%$ ), potassium nitrate ( $\text{KNO}_3$ , Fisher,  $>99.5\%$ ), and DCE (Sigma-Aldrich, HPLC grade) were used as received. Aqueous solutions were prepared from Milli-Q reagent water (Millipore Corp., resistivity  $18.2 \text{ M}\Omega \text{ cm}$  at  $25^\circ\text{C}$ ), while the organic solvent was water-saturated DCE.

**2.2. SECM Setup for Silver Particle Nucleation at the Water/DCE Interface.** A schematic representation of the basic idea behind inducing and monitoring Ag particle nucleation at the water/DCE interface is shown in Figure 1a. An Ag ultramicroelectrode (UME), positioned close to the water/DCE interface, is used to “inject”  $\text{Ag}^+$  ions in a controllable way. At the interface, these electrogenerated  $\text{Ag}^+$  ions react with the DMFc reductant to produce Ag particles. The cylindrical Teflon cell used had a glass body and was fully detachable. It was 4 cm in diameter and had a total volume of about  $25 \text{ cm}^3$ . The cell was filled with aqueous solution and DCE, as the top and bottom phases, respectively. For most experiments, the aqueous phase contained 0.1 M  $\text{LiClO}_4$  and the DCE phase contained 0.03 M DMFc and 0.1 M  $\text{TBAClO}_4$ , except where mentioned otherwise. Electrochemical measurements were made using a two-electrode arrangement. The working electrode was a  $25 \mu\text{m}$  diameter Ag disk UME with an RG value of 10 (ratio of the overall tip radius to that of the silver disk), while a saturated calomel electrode (SCE) served as the reference electrode. Both electrodes were placed in the top aqueous phase. A model 750A bipotentiostat (CH Instrument), controlled by a portable PC, was employed for potentiostatic measurements. The whole setup was shielded by a home-built Faraday cage.

**2.3. Distance Measurements.** The SECM protocol for distance setting between the Ag UME and the L/L interface is shown schematically in Figure 1b, in which oxygen was used as the redox species. By applying a potential of  $-0.8 \text{ V}$  (vs SCE) to the Ag UME for the diffusion-controlled reduction of oxygen, it was possible to accurately determine the distance between the UME and the interface by recording a steady-state current,  $i_t$ , normalized by the steady-state current in bulk solution,  $i_{\text{bulk}}$ , as the tip was translated toward the water/DCE interface. As shown in Figure 2, induced transfer of oxygen from the DCE phase, which acted as a source of  $\text{O}_2$  to the tip

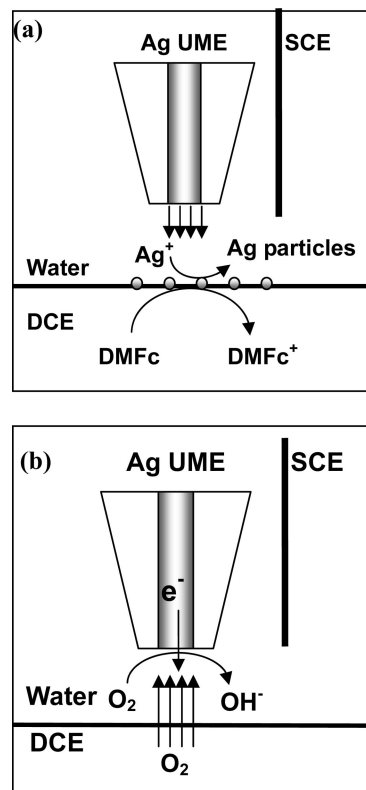


**Figure 1.** Schematic of the SECM setups for (a) Ag particle nucleation at the water/DCE interface and (b) distance setting between the UME and the water/DCE interface.

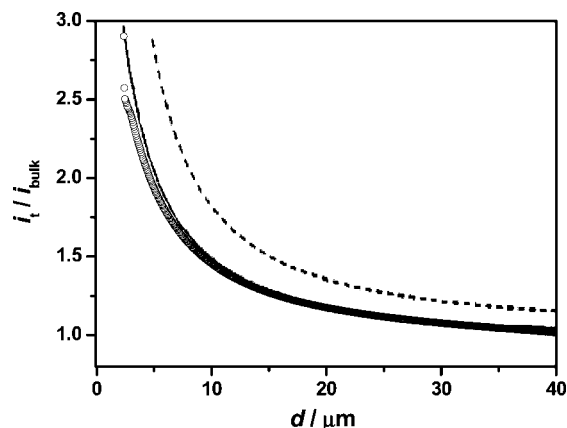


**Figure 2.** Experimental (O) approach curve recorded at a  $25 \mu\text{m}$  diameter Ag UME in an aqueous solution containing 0.1 M  $\text{LiClO}_4$ , translated toward a DCE solution containing 0.03 M DMFc and 0.1 M  $\text{TBAClO}_4$ . The UME potential was  $-0.8 \text{ V}$  (vs SCE) to promote the diffusion-limited reduction of oxygen ( $4\text{-e}^-$  process).<sup>32</sup> The scan speed was  $0.5 \mu\text{m s}^{-1}$ . The solid line corresponds to the theoretical curve for the reduction of oxygen at a tip approaching a water/DCE interface with the parameters defined in the text.<sup>32</sup> The dashed line is the theoretical curve for diffusion-limited infinite-source transfer.<sup>32</sup>

UME, was observed because the concentration and diffusion coefficient of oxygen in the DCE phase ( $c_{\text{O}_2}^{\text{DCE}} = 1.39 \text{ mM}$ ,  $D_{\text{O}_2}^{\text{DCE}} = 2.7 \times 10^{-5} \text{ cm}^2 \text{ s}^{-1}$ )<sup>32</sup> are higher than those in the aqueous phase ( $c_{\text{O}_2}^{\text{aq}} = 0.25 \text{ mM}$ ,  $D_{\text{O}_2}^{\text{aq}} = 2.2 \times 10^{-5} \text{ cm}^2 \text{ s}^{-1}$ ).<sup>32</sup> There is a good match between theory<sup>32</sup> and experiment with the parameters defined. Note that, although transfer of oxygen from DCE enhances the tip current, the DCE phase does not act as an infinite source, so the approach curve current lies below this limiting case (dashed line in Figure 2). Experimental approach curves such as this allowed the distance between tip and

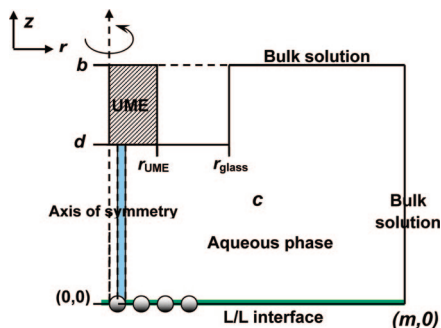


**Figure 3.** Simulation domain and coordinate system for the axisymmetric cylindrical geometry used in the one-domain macroscopic model. Particles are only shown as a guide and are not part of the domain of simulation. The green line represents the domain of simulation for the part of the model concerned with particle size.

interface to be determined precisely. For this particular case, which was typical, the distance of closest approach between the tip and interface was  $2.2 \mu\text{m}$ .

**2.4. Measurements of Redox Potentials.** The redox potentials of  $\text{Ag}/\text{Ag}^+(\text{aq})$  and  $\text{DMFc}/\text{DMFc}^+(\text{DCE})$  needed to estimate driving forces were measured with respect to a common SCE reference electrode (in an aqueous phase). A  $25 \mu\text{m}$  diameter Ag UME was used for the  $\text{Ag}/\text{Ag}^+(\text{aq})$  measurement and the potential was scanned from 0 to 0.40 V to induce the anodic dissolution of the Ag UME. The one-electron oxidation of DME was carried out at a  $25 \mu\text{m}$  diameter Pt UME in a DCE phase ( $0.1 \text{ M TBAClO}_4$ ) with two different concentrations of  $\text{LiClO}_4$  (0.01 and 0.1 M) added to the aqueous phase. The applied potential was scanned from  $-0.4$  to  $0.3 \text{ V}$ .

**2.5. Microscopy Measurements.** Images of Ag particles formed at the water/DCE interface were obtained using a Zeiss LSM 510, Axioplan 2, upright confocal laser scanning microscope (CLSM) with a water immersion objective lens (Zeiss, Achromplan  $20\times/50 \text{ M}$ ) and a  $10\times$  tube lens. Images were processed using the LSM Image Browser software (Zeiss).

An all-glass cylindrical cell was specially designed for the CLSM measurements. It comprised a top glass body (diameter, 4 cm; height, 2.5 cm) and a smaller bottom glass window (diameter, 2 cm; height, 0.8 cm). These two compartments were separated by a glass plate containing a 1 mm-diameter hole where the two liquid phases contacted. A glass tube (diameter, 0.5 cm; height, 2.3 cm) was connected to the lower compartment, so that the level of the bottom phase could be adjusted, if necessary, during the experiments.

The CLSM experiments were performed using a helium/neon laser ( $\lambda = 543 \text{ nm}$ , 100% transmission intensity) and both reflection and transmission modes were employed. The lens of the confocal microscope was dipped into the top phase of the cell to obtain images of the interface.

All experiments were carried out at ambient temperature ( $21 \pm 1^\circ\text{C}$ ) in an air-conditioned room.

### 3. Theory and Simulation

**3.1. Description of Models.** Several models have been proposed for metal deposition processes at solid substrates.<sup>4a,33–38</sup> Herein, the finite element method was used to obtain information on the kinetics of Ag particle formation at the water/DCE interface. We restrict our approach to one phase containing the Ag UME, which is possible because the analysis which follows focuses on conditions where the concentration of DME in DCE,  $c_{\text{DMFc}}$ , was in large excess compared to  $\text{Ag}^+$  ions, and relatively short times were considered where depletion effects in the

second phase would be negligible. The extension to two phases would be straightforward. Two models were involved: first, the growth of Ag particles was described from a macroscopic point of view, and second, a microscopic model was developed to inform the boundary conditions in the macroscopic model.

**3.1.1. Macroscopic Model.** The macroscopic model was used to describe the concentration of  $\text{Ag}^+$  ions in aqueous solution and also the average particle size at the L/L interface. Necessarily, the two parts are coupled through the interfacial flux.

First, the part of the macroscopic model concerned with  $\text{Ag}^+$  ion concentration is considered. The geometry of this part of the model is shown in Figure 3, using axisymmetric cylindrical coordinates. The following diffusion equation was solved on the interior of this domain:

$$D\nabla^2 c = \frac{\partial c}{\partial t} \quad (1)$$

where  $D$  is the diffusion coefficient, and  $c$  is the concentration of  $\text{Ag}^+$  ions in the aqueous solution, which varies both spatially and temporally.

The tip current for the oxidation of the Ag UME is expressed by

$$2n\pi FD \int_0^{r_{\text{UME}}} \left. \frac{\partial c}{\partial z} \right|_{z=d} r dr \quad (2)$$

where  $n$  is the number of electrons transferred ( $n = 1$  for the anodic dissolution of Ag to form  $\text{Ag}^+$  ions),  $F$  is the Faraday constant,  $r$  and  $z$  are the axisymmetric coordinates in the radial and normal directions, respectively,  $r_{\text{UME}}$  is the radius of the Ag UME, and  $d$  is the distance between the Ag UME and the L/L interface. In this case, the diffusion coefficient of  $\text{Ag}^+$  ions in water,  $D$ , was  $1.6 \times 10^{-5} \text{ cm}^2 \text{ s}^{-1}$ .<sup>39</sup> The origin  $(0, 0)$  was chosen to be the intersection of the axis of symmetry of the UME with the L/L interface.

Initially, no  $\text{Ag}^+$  ions are present in solution, therefore

$$t = 0; 0 < r < m; 0 < z < d; c = 0 \quad (3)$$

$$t = 0; r_{\text{glass}} < r < m; d \leq z < b; c = 0 \quad (4)$$

where  $m$  is the radius of the domain of simulation and  $b$  is the distance in the  $z$ -direction to which back-diffusion behind the surface of the UME is considered.

After the potential step ( $t > 0$ ), because the electrogeneration of  $\text{Ag}^+$  ions is electrochemically reversible,<sup>30</sup> the boundary condition at the electrode surface is

$$t > 0; 0 \leq r \leq r_{\text{UME}}; z = d; c = c^* \quad (5)$$

where  $c^*$  is the concentration of generated  $\text{Ag}^+$  ions at the electrode surface (governed by the applied potential). The insulating glass around the electrode is inert to  $\text{Ag}^+$  ions, so

$$t > 0; r_{\text{UME}} < r < r_{\text{glass}}; z = d; D \frac{\partial c}{\partial z} = 0 \quad (6)$$

$$t > 0; r = r_{\text{glass}}; d \leq z < b; D \frac{\partial c}{\partial r} = 0 \quad (7)$$

where  $r_{\text{glass}}$  is the radius of the Ag UME plus glass body. At the axis of cylindrical symmetry, the boundary condition is

$$t > 0; r = 0; 0 \leq z < d; D \frac{\partial c}{\partial r} = 0 \quad (8)$$

Assuming no  $\text{Ag}^+$  ions would reach the edge of the domain in the bulk solution during the experiment,



$$t > 0; r_{\text{glass}} \leq r < m; z = b; c = 0 \quad (9)$$

$$t > 0; r = m; 0 \leq z \leq b; c = 0 \quad (10)$$

At the water/DCE interface, where the deposition of Ag particles occurs, the boundary condition can be written as

$$t > 0; 0 < r < m; z = 0; D \frac{\partial c}{\partial z} = k^*(r_p)c \quad (11)$$

where  $k^*(-)$  is the rate function for particle formation, which is derived in section 3.1.2 from a microscopic model using only the particle average half-spacing,  $L$ , and the rate constant on the surface of the silver particles,  $k$ .  $k^*(-)$  is dependent on the local particle radius function defined on the interface,  $r_p$ , which varies over time as described in section 3.1.3 and is a function of  $r$ , though it is not explicitly written as such.

The experimental results outlined below indicate that there is an additional flux at short times, which we treat as an adsorption process. In this instance, the boundary conditions at the interface (eq 11) is replaced by eq 12.<sup>30</sup>

$$t > 0; 0 < r < m; z = 0; D \frac{\partial c}{\partial z} = k^*(r_p)c + k_{\text{ads}}c(1 - \theta) \quad (12)$$

where  $k_{\text{ads}}$  is the kinetic rate constant for the adsorption process and  $\theta$  is the fraction of adsorption sites occupied with  $\text{Ag}^+$  ions at the L/L interface, a function of  $r$  and  $t$ . The variation of  $\theta$  with time is described by

$$N \frac{\partial \theta}{\partial t} = k_{\text{ads}}c(1 - \theta) \quad (13)$$

where  $N$  is the number of adsorption sites per unit area, which defines a maximum limiting interfacial concentration.

In this model, adsorption and growth processes are treated as parallel. This is reasonable, because they operate on different time scales, as discussed below, with the adsorption process dominating at short times and the growth process becoming increasingly important with time. This formulation is also the simplest and most effective approach to the problem, involving the least number of adjustable parameters. For the simplest case, the UME current–time behavior depends on the distance between the electrode and the L/L interface,  $d$ ; the kinetic rate function,  $k^*(-)$ ; adsorption rate constant,  $k_{\text{ads}}$ ; the electrode surface concentration of electrogenerated  $\text{Ag}^+$  ions,  $c^*$ ; and  $N$ .

The following microscopic model will show how we converted the flux obtained in the microscopic model to a rate constant in the macroscopic simulation.

**3.1.2. Microscopic Model.** The geometry for the microscopic model is shown in Figure 4a, corresponding to the region in the aqueous phase colored blue in the macroscopic model in

Figure 3. Instantaneous nucleation is considered, which is reasonable given that we wish to focus on the initial process and even progressive nucleation collapses to an instantaneous process at sufficiently short times.<sup>40</sup> Furthermore, for externally polarized microscale L/L interfaces, we have shown that Ag nucleation and growth appears to be best described as an instantaneous process.<sup>7</sup> A number of seed particles separated by an average particle–particle spacing of  $2L$  are considered at  $t > 0$ , which are allowed to grow on the basis of the flux to them. Only one cross-section of an Ag particle at the interface is simulated due to the axisymmetric nature of the problem. The steady-state diffusion problem (eq 14) was solved in the interior of this domain.

$$D \nabla^2 c = 0 \quad (14)$$

The tip current for the oxidation of the Ag UME is similar to eq 2, except the domain of integration is restricted only to the portion of UME simulated. The boundary conditions are

$$a < r < L; z = 0; D \frac{\partial c}{\partial z} = 0 \quad (15)$$

$$r = L; 0 \leq z \leq d; D \frac{\partial c}{\partial r} = 0 \quad (16)$$

$$0 \leq r < L; z = d; c = c^* \quad (17)$$

$$r = 0, a < z < d; D \frac{\partial c}{\partial r} = 0 \quad (18)$$

where  $a$  is the radius of the particle.

The boundary condition on the Ag particle surface is expressed by eq 19.

$$0 \leq r \leq a; \\ z = \sqrt{a^2 - r^2}; D \nabla \cdot \mathbf{n} = kc \quad (19)$$

where  $\mathbf{n}$  is the inward pointing unit normal and  $k$  is the rate constant on the surface of the particle.

The flux (as a function of  $a$ ), calculated for the model illustrated in Figure 4a, was used to determine the rate function  $k^*(-)$  (also a function of  $a$ ) necessary to achieve an equivalent flux on the uniformly active surface illustrated in Figure 4b. The derivation is outlined below. Note, to ease notation,  $k^*$  is not explicitly written as a function of  $a$ .

First, the relationship between  $J$ , the total flux in the model in Figure 4b, and the current density at the Ag UME,  $j$ , is given by

$$J = \pi L^2 j \quad (20)$$

In this system,  $j$  is dependent on the reaction rate function  $k^*$  by

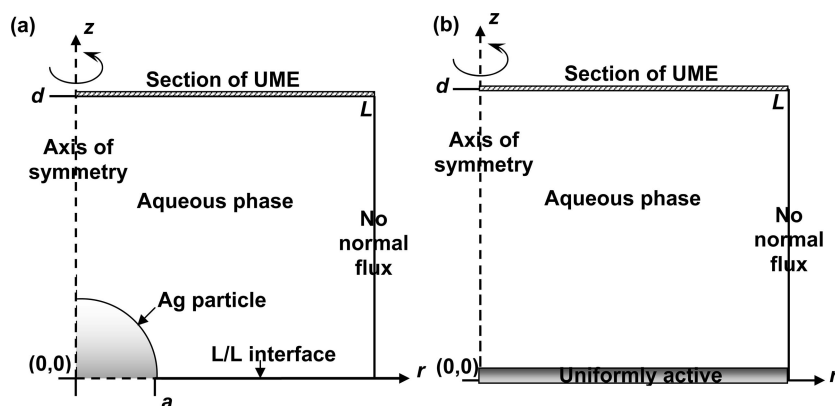


**Figure 4.** (a) Simulation domain and coordinate system for the axisymmetric cylindrical geometry used in the microscopic model and (b) the domain for a flat interface, with a layer of Ag particle formed, to which the model is equated.

$$j = D \left( \frac{c^* - c^{\text{inter}}}{d} \right) = k^* c^{\text{inter}} \quad (21)$$

where  $c^{\text{inter}}$  is the concentration of  $\text{Ag}^+$  ions at the water/DCE interface. From eq 21,  $k^*$  can be expressed by

$$k^* = \frac{D}{c^{\text{inter}}} \left( \frac{c^* - c^{\text{inter}}}{d} \right) \quad (22)$$

Combining eqs 20 and 21,

$$\frac{J}{\pi L^2} = D \left( \frac{c^* - c^{\text{inter}}}{d} \right) \quad (23)$$

Then from eq 23,  $c^{\text{inter}}$  is given by

$$c^{\text{inter}} = c^* - \frac{Jd}{D\pi L^2} \quad (24)$$

Inputting eq 24 into eq 22, the relationship between  $k^*$  and  $J$  is written as

$$k^* = \frac{D}{\left( c^* - \frac{Jd}{D\pi L^2} \right)} \left[ \frac{c^* - \left( c^* - \frac{Jd}{D\pi L^2} \right)}{d} \right] \quad (25)$$

Eq 25 is further simplified to

$$k^* = \frac{JD}{D\pi L^2 c^* - Jd} \quad (26)$$

Many simulations were performed using the model illustrated in Figure 4a. The corresponding fluxes were used to determine  $k^*(-)$  as a function of  $a$ , which was implemented in the macroscopic model using an interpolating function.

**3.1.3. Particle Growth Application Mode.** As described above, the boundary conditions at the L/L interface are dependent on the particle size. A set of equations are described below which relate the flux at the L/L interface to the average particle size, which is a function of  $r$  and time ( $t$ ). For ease of notation, the dependence on  $r$  is dropped.

Both the volume and radius of the Ag particle formed are dependent on time ( $t$ ):

$$\text{Vol}(t) = \frac{4}{3} \pi a(t)^3 \quad (27)$$

Then, it follows that

$$\frac{d\text{Vol}(t)}{dt} = 4\pi a(t)^2 \frac{da(t)}{dt} \quad (28)$$

So

$$\frac{da(t)}{dt} = \frac{1}{4\pi a(t)^2} \frac{d\text{Vol}(t)}{dt} \quad (29)$$

The rate of volume change is proportional to the flux to the particle, so in our situation

$$\frac{d\text{Vol}(t)}{dt} = \frac{1}{\rho} AD \left. \frac{\partial c}{\partial z} \right|_{z=0} \quad (30)$$

where  $\rho$  is the Ag molar density, which was calculated from the Ag density<sup>41</sup> as  $97.3 \text{ mol dm}^{-3}$ , and  $A$  is the whole area of a single particle at the interface, which is equal to  $\pi L^2$ . Thus,

$$\frac{da(r, t)}{dt} = \frac{A}{4\pi a(r, t)^2 \rho} D \left. \frac{\partial c(r, z, t)}{\partial z} \right|_{z=0} \quad (31)$$

According to eq 31, the rate of change of the particle radius can be deduced from the interfacial flux.

The mass transport problem outlined was modeled using a commercial finite element method modeling package (Comsol Multiphysics, version 3.3a), in conjunction with MATLAB [version 7.4.0 (R2007a)]. This was run on a Dell desktop PC (4 GB RAM and a 2.52 GHz Pentium 4 Processor) running Windows XP. The problem was solved in real space to allow direct analysis of the experimental data. In the model described, the distances into which bulk solution was simulated, i.e.,  $m$  and  $b$ , were empirically determined by running simulations of increasingly large domain until no change in the tip current was observed. The number and density of mesh elements were again determined heuristically, through successive refinements of the mesh until no change in the current was observed.

**3.2. Theoretical Results and Discussion.** As stated above, the anodic tip current response is sensitive to the interaction of  $\text{Ag}^+$  ions with the water/DCE interface, notably the rate constant for Ag particle growth at the particle surface,  $k$ ; the concentration of generated  $\text{Ag}^+$  ions at the electrode surface,  $c^*$ ; the tip–interface separation,  $d$ ; and the average particle–particle half-spacing,  $L$ . The aim of this section is to analyze the Ag particle nucleation process on the basis of the theoretical models developed above and to examine the effects of the above parameters on the tip current response. As discussed, a relatively short time scale of 1 s was considered to simplify the analysis.

**3.2.1. Ag Particle Growth at the Interface with Time.** First, we consider an example of the current–time characteristics of a series of typical parameters, specifically a large rate constant,  $k = 10 \text{ cm s}^{-1}$ ,  $c^* = 1.0 \text{ mM}$ ,  $d = 4 \mu\text{m}$ , and  $L = 7 \times 10^{-5} \text{ cm}$ . A typical simulated current–time curve is shown in Figure 5 and is compared to the limiting behavior for an inert interface. Initially, the behavior is similar to that for an inert interface, since the electrogenerated  $\text{Ag}^+$  ions in the aqueous phase have to diffuse to the L/L interface, nucleate Ag particles, and then grow, consuming an increasing flux of  $\text{Ag}^+$  ions with time. At longer times, specifically after 0.03 s, the formation of Ag particles at the L/L interface from the reaction between generated  $\text{Ag}^+$  ions and DMFc causes the flux of  $\text{Ag}^+$  ions to the L/L interface to increase, resulting in an enhancement of the tip current with time.

Figure 6 shows a sequence of concentration profiles of electrogenerated  $\text{Ag}^+$  ions in the aqueous solution,  $c$ , in a small domain below the electrode ( $d = 4 \mu\text{m}$ ) for three simulation times, corresponding to the points labeled 1, 2, and 3 in Figure 5 (N.B., length scales are different on the  $r$  and  $z$  axes). In Figure

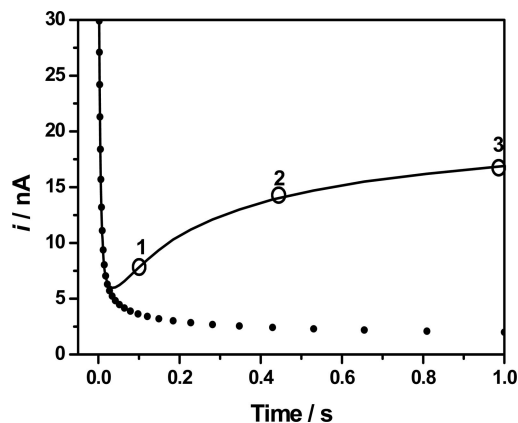


**Figure 5.** Simulated current–time characteristics (solid curve) over a period of 1 s for a growth process characterized by  $k = 10 \text{ cm s}^{-1}$ ,  $c^* = 1.0 \text{ mM}$ ,  $d = 4 \mu\text{m}$ , and  $L = 7 \times 10^{-5} \text{ cm}$ . The dotted curve is the theoretical curve corresponding to no growth process ( $k = 0$ ), i.e., an inert interface. Labels 1, 2, and 3 represent times of 0.1, 0.43, and 1 s, respectively.

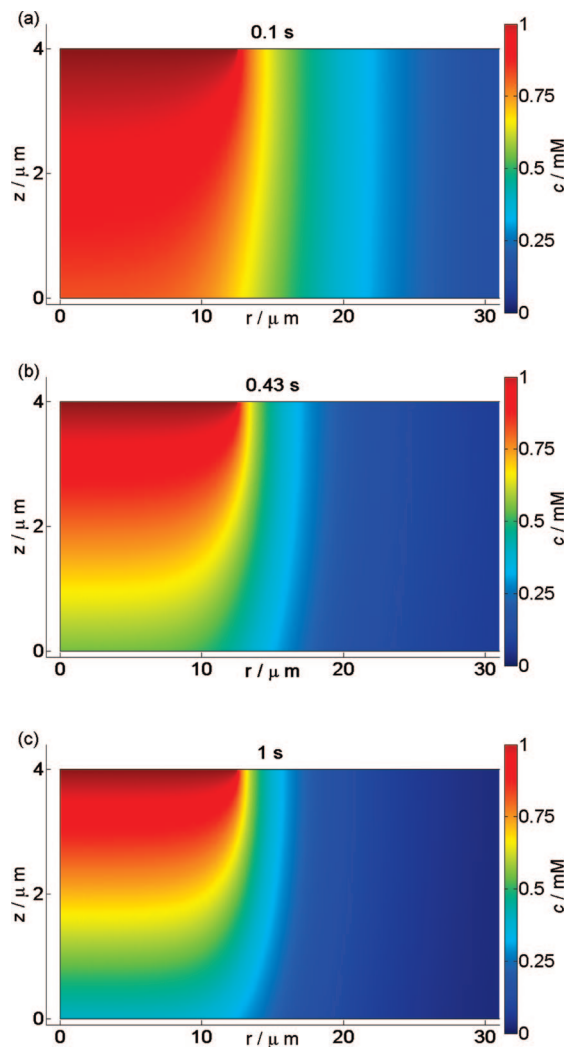


**Figure 6.** Simulated concentration profiles for electrogenerated  $\text{Ag}^+$  ions,  $c$ , in the aqueous phase at time scales of (a) 0.1 s, (b) 0.43 s, and (c) 1 s. The parameters used for simulation were the same as for Figure 5. N.B., horizontal and vertical length scales are not in proportion.

6a, corresponding to a short time of 0.1 s,  $c$  decreases only slightly from its defined value at the tip surface ( $c^* = 1.0$  mM) to about 0.8 mM at the part of the interface directly under the center of the tip. There is also some lateral dispersion of  $\text{Ag}^+$  ions, because of the small interfacial flux of  $\text{Ag}^+$  ions used to form Ag particles at the L/L interface at this short time. With prolonged simulation time, a more extensive decrease of  $c$  at the L/L interface can be seen in Figure 6b,c, with values of  $c$  at the part of the interface directly below the tip of about 0.5 and 0.4 mM, respectively, for 0.43 and 1 s. The corresponding steepening of the concentration profiles, due to the consumption of  $\text{Ag}^+$  ions in the nucleation and growth process, is reflected in the enhanced tip currents at these times. It should be noted that at a time of 1 s, the flux of  $\text{Ag}^+$  ions is highly focused toward a portion of the interface that approximates the UME size. This has implications for the long-time form of experimental transients, at long times, reported later (see sections 4.1 and 4.2).

The model also provides information on the particle size distribution at the interface with time. Figure 7 shows the particle radius,  $r_p$ , as a function of radial distance,  $r$ , at the interface at several simulation times (0.1, 0.43, and 1 s). For each time, as the radial distance,  $r$ , increases, there is a gradual decrease of  $r_p$ , which is because particle nucleation and growth occur most

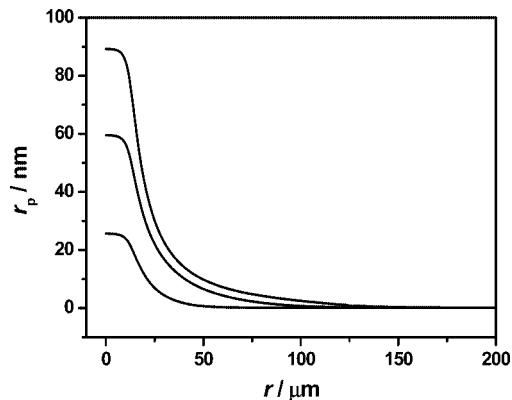


**Figure 7.** Simulated radius of particles formed at the interface,  $r_p$ , as a function of radial distance,  $r$ , for different times. From bottom to top, the simulation times were 0.1, 0.43, and 1 s, respectively. The simulation parameters used were as for Figure 5.

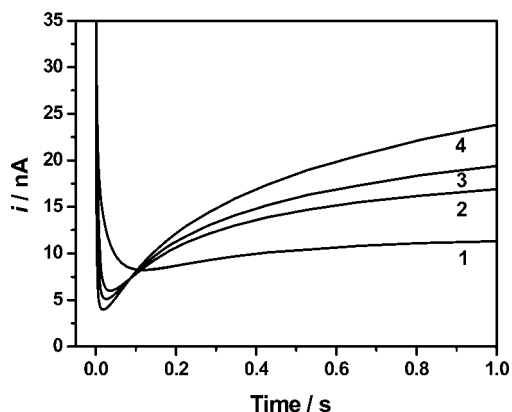


**Figure 8.** Simulated current-time curves over a time period of 1 s for tip-interface separations,  $d$ , of (1) 10  $\mu\text{m}$ , (2) 4  $\mu\text{m}$ , (3) 3  $\mu\text{m}$ , and (4) 2  $\mu\text{m}$ . Other simulation parameters were  $k = 10$   $\text{cm s}^{-1}$ ,  $c^* = 1.0$  mM, and  $L = 7 \times 10^{-5}$  cm.

significantly in the region of the L/L interface closest to the location of the UME. With prolonged simulation times, the particle radius becomes greater and particles grow to some extent in a larger portion of the interface. However, in general, the simulation result further confirms that the growth process is largely confined to a region of the L/L interface similar in size to the UME.

The data in Figure 7 also allow one to estimate the frequency of  $\text{Ag}^+$  addition to particles. Given  $r_p$  values in the region directly under the tip of ca. 25, 60, and 90 nm at 0.1, 0.43, and 1 s, respectively, the average addition rate to a single particle is  $3.8 \times 10^7$  atoms/s (in the period up to 0.1 s),  $1.5 \times 10^8$  atoms/s (for 0.1–0.43 s), and  $2.2 \times 10^8$  atoms/s (0.43–1 s). These values are typical of those found experimentally in the studies reported below. Note that the largest particle in Figure 7 (at 1 s) is approximately 90 nm radius. With an interparticle half-spacing of  $7 \times 10^{-5}$  cm, this means that only ca. 0.6% of the interfacial area is covered by Ag particles. This highlights that it was not necessary to consider any reduction in the L/L interfacial area (for the adsorption process) as a consequence of the growth process.

**3.2.2. Effect of Tip-Interface Distance.** The effect on the tip current-time response of varying the tip-interface distance,  $d$ , while other parameters are kept constant, is shown in Figure 8 for  $k = 10$   $\text{cm s}^{-1}$ ,  $c^* = 1.0$  mM, and  $L = 7 \times 10^{-5}$  cm. The general form of the transients was explained above in the discussion of Figure 5. In Figure 8, it can be seen that decreasing the tip-interface separation,  $d$ , causes a larger difference

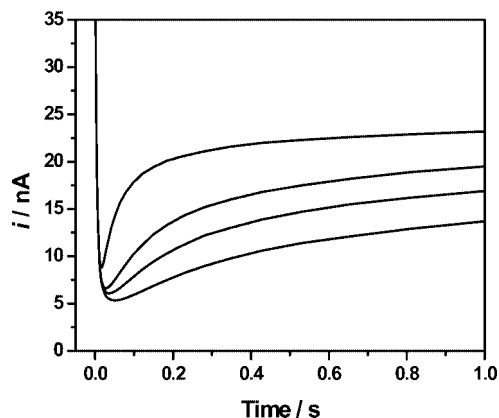


**Figure 9.** Simulated current–time curves over a period of 1 s for several values of the particle–particle half-spacing,  $L$ . From bottom to top, the values of  $L$  were  $1 \times 10^{-4}$ ,  $7 \times 10^{-5}$ ,  $5 \times 10^{-5}$ , and  $2 \times 10^{-5}$  cm, respectively. Other simulation parameters were  $k = 10 \text{ cm s}^{-1}$ ,  $c^* = 1.0 \text{ mM}$ , and  $d = 4 \text{ }\mu\text{m}$ .

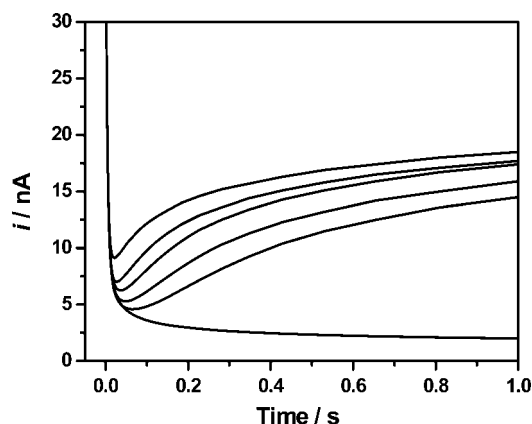


**Figure 10.** Simulated current–time curves over a time period of 1 s for several rate constants,  $k$ , for Ag particle growth. From bottom to top, the values of  $k$  were 0, 4, 6, 10, 20, and  $1000 \text{ cm s}^{-1}$ , respectively. Other parameters were  $c^* = 1.0 \text{ mM}$ ,  $d = 4 \text{ }\mu\text{m}$ , and  $L = 7 \times 10^{-5} \text{ cm}$ .

between the current extremes for an essentially inert surface at short times and an active (sink) surface at longer times. This is because the smaller the value of  $d$ , the higher the mass transport challenge on the interface, as evident in earlier SECM transient studies of interfacial reactivity.<sup>42,43</sup>

**3.2.3. Effect of Particle–Particle Half-Spacing.** The particle–particle half-spacing,  $L$ , is also a very important parameter for this system. A large value of  $L$  corresponds to a small density of nucleation sites, and this naturally means the net growth process is less extensive, for a given rate constant, certainly at short times. Figure 9 shows simulated current–time curves for four different values of  $L$  ( $1 \times 10^{-4}$ ,  $7 \times 10^{-5}$ ,  $5 \times 10^{-5}$ , and  $2 \times 10^{-5} \text{ cm}$ ). As expected, at any time after the  $\text{Ag}^+$  ion diffusion field has intercepted the L/L interface, decreasing  $L$  has the effect of increasing the tip current. Furthermore, the smaller the value of  $L$ , the more sharply the tip current increases during the growth phase.

**3.2.4. Effect of Reaction Rate Constant.** The reaction rate constant for Ag growth at the particle surface,  $k$ , clearly determines the growth rate and thus the form of the tip current transient. This can be seen in Figure 10, in which the tip current–time response was simulated for six reaction rate constants, including a value close to the limit of most rapid growth ( $k = 1000 \text{ cm s}^{-1}$ ) and no growth ( $k = 0$ ). The tip current increases with  $k$ , because  $k$  controls the rate of growth of Ag

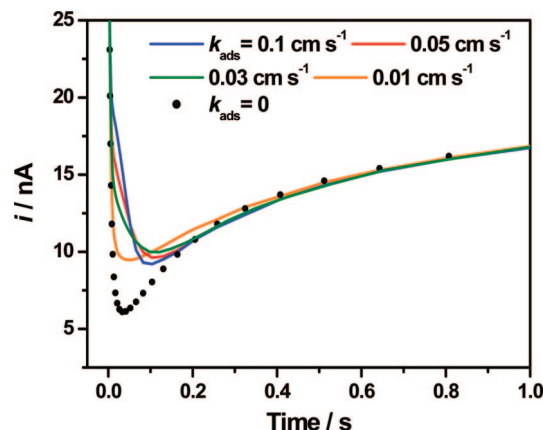


**Figure 11.** Simulated current–time curves over a time period of 1 s for several values of  $k_{\text{ads}}$  (shown in the figure). Other parameters were  $k = 10 \text{ cm s}^{-1}$ ,  $c^* = 1.0 \text{ mM}$ ,  $d = 4 \text{ }\mu\text{m}$ ,  $L = 1.0 \times 10^{-4} \text{ cm}$ , and  $N = 9 \times 10^{-10} \text{ mol cm}^{-2}$ . The limiting case of no adsorption is shown by the dotted curve.

particles at the water/DCE interface, leading to an enhancement of the flux of electrogenerated  $\text{Ag}^+$  ions away from the tip electrode. It can be seen that the tip current is rather sensitive to the rate constant over a wide range of values (see caption to Figure 10). Significantly, large rate constants can be characterized by this technique, because the initial nuclei are so small that the mass transport rate to individual particles is extremely high.

**3.2.5. Effect of  $\text{Ag}^+$  Ion Adsorption at the Interface.** In the light of the experimental results which follow, the effect of the adsorption of  $\text{Ag}^+$  ions at the L/L interface on the tip current response was examined. The treatment which follows is general and could involve electron transfer coupled to adsorption as well as simple adsorption. As stated in section 3.1.1, two parameters are used to quantify the adsorption process: the adsorption rate constant,  $k_{\text{ads}}$ , and the adsorption sites per unit area,  $N$ . It is reasonable to consider an essentially irreversible process, because the adsorption process will be driven in that direction by the electrogenerated flux of  $\text{Ag}^+$  ions toward the L/L interface. The effect of  $k_{\text{ads}}$  was studied in this section with  $N = 9 \times 10^{-10} \text{ mol cm}^{-2}$ , which would be consistent with (maximum) monolayer coverage. Typical current–time curves are shown in Figure 11 for an adsorption process with  $k_{\text{ads}}$  in the range  $0.01 \text{ cm s}^{-1}$  to  $0.1 \text{ cm s}^{-1}$ , coupled to nucleation and growth characterized by  $k = 10 \text{ cm s}^{-1}$  and  $L = 1.0 \times 10^{-4} \text{ cm}$ . The other parameters were  $c^* = 1.0 \text{ mM}$  and  $d = 4 \text{ }\mu\text{m}$ . For comparative purposes, data are also shown for  $k_{\text{ads}} = 0$ . It can be seen that adsorption causes the minimum in the  $i$ – $t$  curves to be much less pronounced, because adsorption provides an extra sink of the ion flux from the electrode. With a faster adsorption process, there is an increasingly pronounced current enhancement at the shortest times ( $t < 0.05 \text{ s}$ ) and the minimum in the  $i$ – $t$  curve actually shifts to longer times, compared to the case shown with no adsorption. It is important to note that, at long times, the adsorption process is essentially complete, and this portion of the  $i$ – $t$  curve ( $t > 0.4 \text{ s}$ ) is similar for all cases.

## 4. Experimental Results and Discussion

### 4.1. Growth of Ag Particles at the Water/DCE Interface.

Metal deposition occurs at L/L interfaces by an interfacial reduction process between a metal precursor located in the aqueous phase and a reductant in the organic phase. Given a suitable interfacial potential difference, heterogeneous electron



transfer from the organic reductant to the aqueous metal ion takes places, leading to the electrodeposition of a metal phase at the interface. In this system, the difference of the redox potentials of the aqueous (aq)  $\text{Ag}/\text{Ag}^+$  couple and organic (o)  $\text{DMFc}/\text{DMFc}^+$  couple drives the interfacial reduction of the aqueous phase silver ion to solid metallic silver at the interface (i). The net process is:



The large difference in the standard potentials of the two redox couples suggests that this electron transfer reaction may occur spontaneously when the two phases are brought into contact. This was readily proven: when an aqueous solution containing 1 mM  $\text{AgNO}_3$  and 0.1 M  $\text{LiClO}_4$  was shaken with a DCE solution containing 2 mM  $\text{DMFc}$  and 0.1 M  $\text{TBAClO}_4$  for about 30 s, a dark layer formed at the interface, evident of Ag formation. The DCE solution changed from yellow to the green after the reaction, which indicates the production of  $\text{DMFc}^+$  from the yellow-colored  $\text{DMFc}$ .

In the SECM experiments,  $\text{Ag}^+$  ions in the aqueous phase were provided by applying an appropriate oxidation potential to the UME probe:



The flux of electrogenerated  $\text{Ag}^+$  ions from the UME surface was partly determined by the applied potential at the electrode, since this controlled the surface concentration  $c^*$ , based on eq 34

$$E_{\text{Ag}/\text{Ag}^+} = E_{\text{Ag}/\text{Ag}^+}^{\circ'} + \frac{RT}{F} \ln c^* \quad (34)$$

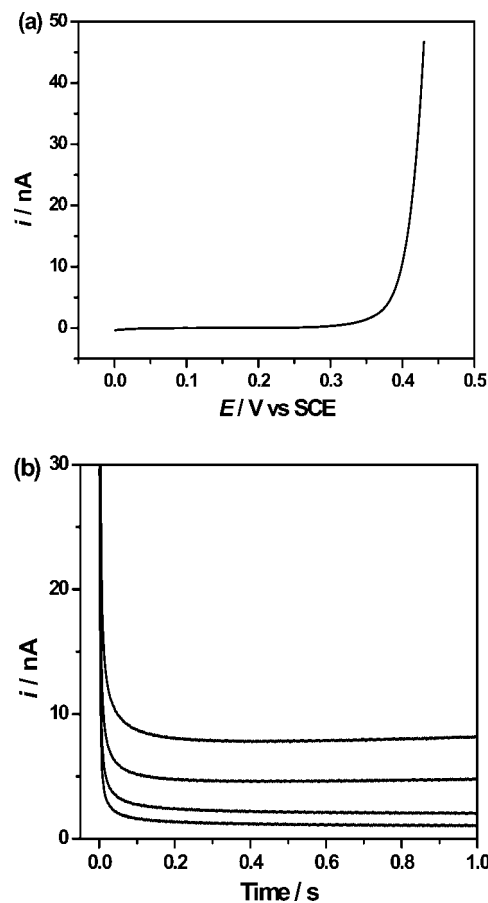
where  $E_{\text{Ag}/\text{Ag}^+}$  is the potential applied to the electrode,  $E_{\text{Ag}/\text{Ag}^+}^{\circ'}$  is the formal potential for the  $\text{Ag}/\text{Ag}^+$  couple, and  $R$  and  $T$  are the gas constant and temperature, respectively.

Figure 12a is a linear sweep voltammogram of Ag oxidation at the Ag UME in the aqueous solution. A significant oxidation current flows at potentials more anodic than 0.3 V; we have previously shown the response to be Nernstian.<sup>30,44</sup> Figure 12b is a series of current–time curves, obtained by stepping the potential from a value where no current flowed to various anodic values. In each case, immediately after the potential step, the UME current starts high and rapidly decays to a steady-state potential-dependent value. The transients for this process have the form of a diffusion-controlled process.<sup>30,44</sup> From these responses, the steady-state limiting currents, recorded at the Ag UME with different applied potentials in the bulk solution ( $i_{\text{bulk}}$ ), could be obtained, from which the corresponding electrode surface concentrations were deduced from eq 35

$$i_{\text{bulk}} = 4nFDr_{\text{UME}}c^* \quad (35)$$

The resulting plot of  $E_{\text{Ag}/\text{Ag}^+}$  vs  $\ln(c^*)$ , shown in Figure 13, is linear with a slope of 0.0244 V, close to the value of  $RT/F$  at 22 °C, 0.025 V. This analysis, and our earlier work,<sup>30,44</sup> demonstrates that the  $\text{Ag}/\text{Ag}^+$  couple is reversible on the SECM spatiotemporal scale.

To minimize the effect of the diffusion of the organic electron donor  $\text{DMFc}$  on the kinetics of the overall reaction, the concentration of  $\text{DMFc}$  ( $c_{\text{DMFc}}$ ) in the DCE phase was kept in significant excess over that of  $\text{Ag}^+$  ions ( $c$ ) in the aqueous phase and the quantitative analysis of current–time curves focused on short times, i.e., on the initial nucleation and growth phase, as stated in the theory section. This time region was most compatible with the assumptions and simplifications of the model, which considered instantaneous nucleation of well-



**Figure 12.** (a) Voltammogram of Ag oxidation from a 25  $\mu\text{m}$ -diameter Ag disk-UME in an aqueous solution containing 0.1 M  $\text{LiClO}_4$ . The scan rate was 20  $\text{mV s}^{-1}$ . (b) Current–time curves recorded at the Ag UME in bulk solution with different applied potentials of 0.34, 0.36, 0.38, and 0.39 V (vs SCE) (from bottom to top).

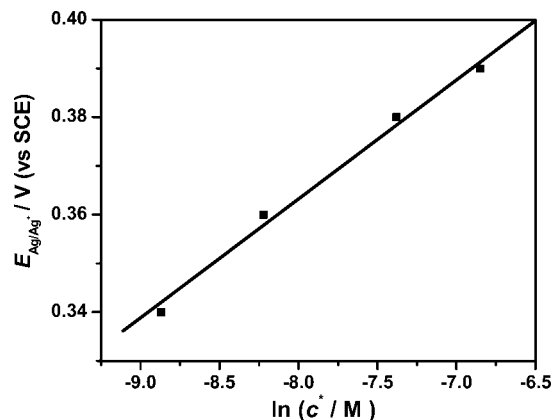


**Figure 13.** Plot of  $E_{\text{Ag}/\text{Ag}^+}$  vs  $\ln(c^*)$ .

defined spherical particles. The transfer of the common ion of the supporting electrolytes in the two phases,  $\text{ClO}_4^-$ , across the interface maintained electroneutrality.

After positioning the Ag UME very close to the water/DCE interface (as described in the Experimental Section), a chronoamperometric measurement of Ag anodic dissolution was made by applying a potential step from 0 V to the desired potential, recorded over a period of 2 s. Typical results are shown in Figure 14 for the cases with  $\text{DMFc}$  in the DCE phase (top curve) and without (bottom curve). The experimental current flow reflects the rate of diffusion of  $\text{Ag}^+$  ions from the electrode and the interaction of  $\text{Ag}^+$  ions with the interface. When  $\text{DMFc}$  is in

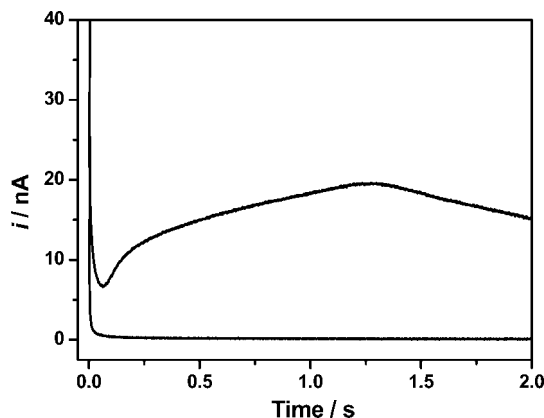


**Figure 14.** Current–time transients recorded at a 25  $\mu\text{m}$  diameter Ag UME in an aqueous solution with a potential step from 0 to 0.39 V (vs SCE). The aqueous solution contained 0.1 M  $\text{LiClO}_4$  and the DCE phase contained 0.1 M  $\text{TBAClO}_4$  with 0.03 M DMFc (top curve) and without DMFc (bottom curve). The distance between the UME and interface was 3.8  $\mu\text{m}$  (with DMFc) and 4.5  $\mu\text{m}$  (without DMFc).

the DCE phase, the current response of the UME is linked particularly to the process of Ag particle nucleation at the L/L interface, as discussed earlier. Except at the very shortest times, when the  $\text{Ag}^+$  ion flux from the UME has not interacted with the L/L interface, the current response (top curve) is always higher than that for an inert interface (bottom curve). In the latter case, the response simply reflects the hindered diffusion of  $\text{Ag}^+$  away from the UME, without any interaction with the L/L interface.

It is interesting to note that at about 1.2 s for the situation with DMFc (top curve), the current reaches a maximum value and then decreases. We attribute this to the Ag growth process at the L/L interface becoming partly limited by the concentration of DMFc in the DCE phase which, even though at high concentration, gradually becomes depleted.

As discussed in section 3.2.1, Ag deposition occurs at a spot with dimensions that approximate to the size of the electrode. The absolute maximum current that DMFc can sustain is  $4nFD_{\text{DMFc}}C_{\text{DMFc}}\gamma$  (where  $\gamma$  is radius of the Ag deposit), which is about 100 nA. In Figure 14, the highest tip current recorded for the generation of  $\text{Ag}^+$  ions is about 20 nA, which is around 20% of the maximum current that DMFc can sustain. Thus, the formation of Ag particles at the interface causes the local depletion of DMFc in the DCE phase.

**4.2. Effects of Experimental Parameters on the Kinetics of Ag Particle Nucleation at the Interface.** **4.2.1. Effect of Tip–Interface Distance.** To be most sensitive to Ag particle nucleation at the water/DCE interface, the SECM tip should be placed close to the interface,<sup>30</sup> as discussed earlier in the theoretical section. Current–time transients for  $\text{Ag}^+$  electro-generation at different tip–interface distances (in the range of 9.2 to 3.8  $\mu\text{m}$ ), depicted in Figure 15, confirm this aspect experimentally. The data in Figure 15 show that the tip current response becomes most sensitive to the interfacial process (most pronounced current minimum at short times; highest current at longer times) as the tip–interface separation decreases. This is entirely consistent with the simulation results presented above.

As discussed in the theory and simulation section, the closer the tip–interface separation, the greater the mass transport challenge provided by the SECM technique and so the lower the current value attained during the period of initial nucleation. Then, as the particles grow, the current increases steeply with time, because the growth flux becomes increasingly strong. By contrast, at greater tip–interface separations, these effects—the

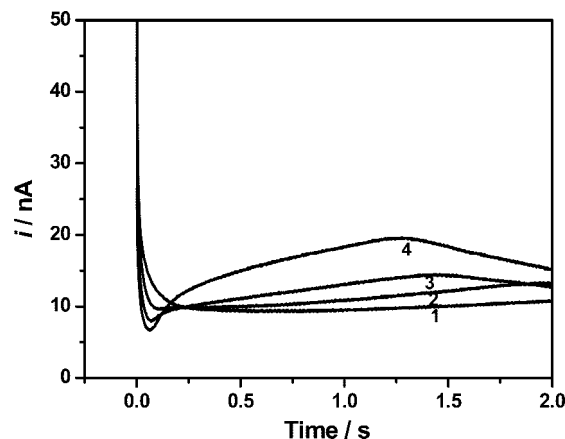


**Figure 15.** Current–time transients recorded at a 25  $\mu\text{m}$  diameter Ag UME in an aqueous solution as a function of the tip–interface separation. The aqueous phase contained 0.1 M  $\text{LiClO}_4$  and the DCE phase contained 0.03 M DMFc and 0.1 M  $\text{TBAClO}_4$ . The UME potential was stepped from 0 to 0.39 V (vs SCE). From curve 1 to 4, the tip–interface separations were 9.2, 7.3, 5.8, and 3.8  $\mu\text{m}$ , respectively.

minimum and the rise in current—are somewhat washed out, as the lower mass transport (challenge) does not place such demands on the interfacial process. Clearly, the closer the tip–interface separation, the earlier and greater the maximum in the current response before a longer time decline is observed, due to DMFc depletion in the DCE phase, which leads to a diminution of the growth flux. It can be seen in Figure 15 that the current decrease in this time domain is most significant for the closer tip–interface separations (3.8 and 5.8  $\mu\text{m}$ ), whereas it is barely evident for the larger tip–interface separations (7.3 and 9.2  $\mu\text{m}$ ).

The data in Figure 15 highlight the sensitivity of this method for following interfacial Ag deposition. On the basis of this experiment, a typical tip–interface separation in the range 3–5  $\mu\text{m}$  was chosen in most of the SECM experiments that follow, to ensure the current response was sufficiently sensitive to the nucleation and growth process.

**4.2.2. Effect of the Applied UME Potential.** Figure 16a shows current–time transients recorded at the Ag UME with different potentials of 0.37, 0.38, 0.39, and 0.4 V applied to the UME. As shown in the figure, the transient current responses show a marked dependence on the applied potential: notably, following the initial minimum, the current increases earlier and more steeply, the greater the applied potential. This is because the greater the applied potential, the higher the flux of  $\text{Ag}^+$  ions delivered from the UME probe to the interface. Furthermore, the greater the applied electrode potential, the earlier the peak current before the long time current decay corresponding to the onset of DMFc depletion in the DCE phase.

By fitting the early part of the experimental curves with the numerical model highlighted in section 3, the nature of the nucleation process at the L/L interface can be analyzed quantitatively. Simulation results are shown in Figure 16b alongside the experimental data. The analysis focused on the first 1 s of the transients to ensure that DMFc depletion and Ag aggregate formation would be negligible. The UME surface concentration of  $\text{Ag}^+$  ions was determined from the applied potential according to eq 34, and the accurate tip–interface separation used for simulation was determined from the oxygen reduction current, in steady-state approach curve positioning, as described above.

In the simulation, the rate constant for Ag particle growth,  $k$ , and the particle–particle half-spacing,  $L$ , were variables in fitting

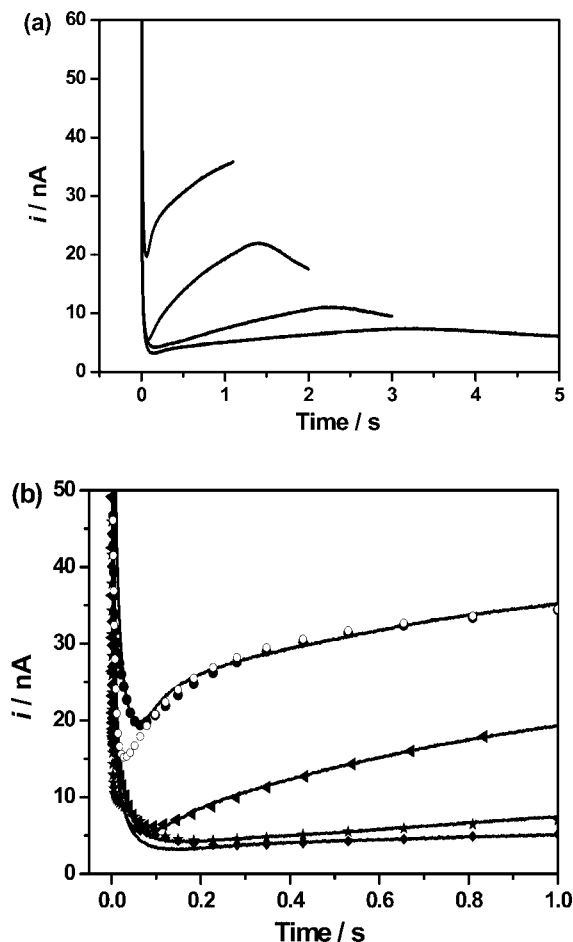


**Figure 16.** (a) Current–time transients recorded at a 25  $\mu\text{m}$  diameter Ag UME with different applied potentials (vs SCE) giving  $c^*$  values of 0.42, 0.59, 1.0, and 1.95 mM (from bottom to top). The aqueous solution contained 0.1 M  $\text{LiClO}_4$  and the DCE phase contained 0.03 M DMFc and 0.1 M TBAClO<sub>4</sub>. From bottom to top, the distances between the UME and interface were 3.5, 3.1, 3.4, and 4.6  $\mu\text{m}$ , respectively. (b) Simulations of the experimental tip currents in part a over a time scale of 1.0 s (solid symbols). The parameters providing the best fit between the experimental and simulated curves were (◆)  $L = 1.0 \times 10^{-4}$  cm ( $d = 3.5$   $\mu\text{m}$ ), (★)  $L = 9.7 \times 10^{-5}$  cm ( $d = 3.1$   $\mu\text{m}$ ), (▲)  $L = 8.0 \times 10^{-5}$  cm ( $d = 3.4$   $\mu\text{m}$ ), and (●)  $L = 6.0 \times 10^{-5}$  cm ( $d = 4.6$   $\mu\text{m}$ ). Other parameters used for the simulations were  $k = 10$  cm s<sup>−1</sup>,  $k_{\text{ads}} = 0.05$  cm s<sup>−1</sup>,  $N = 9 \times 10^{-10}$  mol cm<sup>−2</sup>, and  $D_{\text{Ag}^+} = 1.60 \times 10^{-5}$  cm<sup>2</sup> s<sup>−1</sup>. The curve comprised of open circles is the simulation for an applied tip potential of 0.40 V, but with  $k_{\text{ads}}$  and  $N$  set to zero.

the data. The influence of these two parameters on the current–time behavior is sufficiently different to allow a unique fit. In Figure 16b, from bottom to top, with increasing potential applied at the Ag UME, the value of  $k$  was obtained as a constant, 10 cm s<sup>−1</sup>, and the value of  $L$  decreased slightly from  $1.0 \times 10^{-4}$  to  $6 \times 10^{-5}$  cm. Although there is a small variation in  $d$  (see the caption to Figure 16a, this trend can be rationalized because the greater the initial  $\text{Ag}^+$  ion flux from the UME to the L/L interface, the higher the probability of Ag particle formation, leading to a decrease of spacing between nuclei ( $L$ ) formed at the interface. On the other hand,  $k$  is related to the rate of  $\text{Ag}^+$  ion discharge at a growing particle. Beyond ultrasmall particles, this would be expected to be independent of particle size and spacing.

It is important to note that the experiments could not be modeled without considering an initial adsorption of  $\text{Ag}^+$  ions at the interface. Take the experimental curve of 0.40 V as an

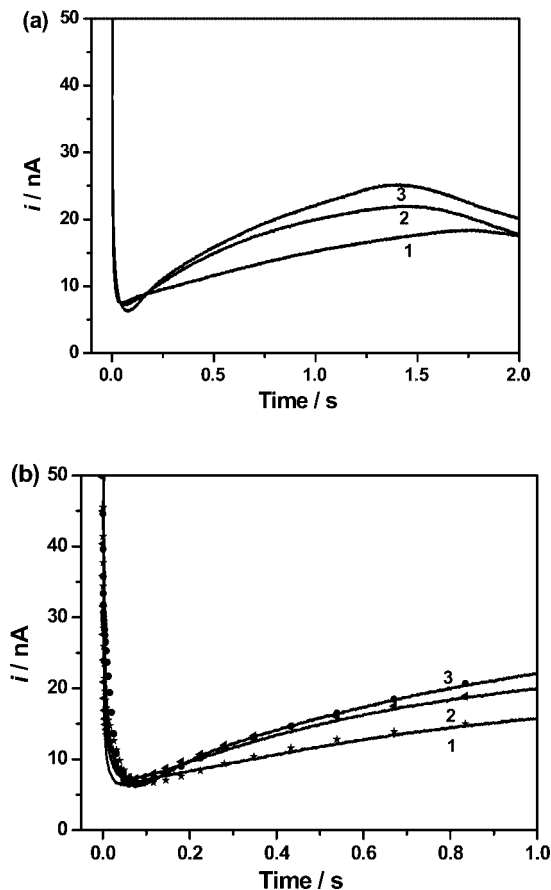


**Figure 17.** (a) Current–time transients recorded at a 25  $\mu\text{m}$  diameter Ag UME with different concentrations of DMFc in DCE. The aqueous solution contained 0.1 M  $\text{LiClO}_4$  and the DCE phase contained 0.1 M TBAClO<sub>4</sub> and 0.01, 0.02, and 0.03 M DMFc (curves 1, 2, and 3, respectively). The distances between the UME and L/L interface were 4.0, 2.5, and 3.4  $\mu\text{m}$ , respectively. The UME potential was stepped from 0 to 0.39 V (vs SCE). (b) Simulations of the experimental tip currents in part a over a time scale of 1.0 s (solid symbols). The parameters providing the best fit between the experimental and simulated curves were (★)  $k = 5$  cm s<sup>−1</sup>,  $L = 7.0 \times 10^{-5}$  cm ( $d = 4.0$   $\mu\text{m}$ ), (▲)  $k = 7$  cm s<sup>−1</sup>,  $L = 8.0 \times 10^{-5}$  cm ( $d = 2.5$   $\mu\text{m}$ ), and (●)  $k = 10$  cm s<sup>−1</sup>,  $L = 8.0 \times 10^{-5}$  cm ( $d = 3.4$   $\mu\text{m}$ ). Other parameters used for the simulations were  $c^* = 1.0$  mM,  $k_{\text{ads}} = 0.05$  cm s<sup>−1</sup>,  $N = 9 \times 10^{-10}$  mol cm<sup>−2</sup>, and  $D_{\text{Ag}^+} = 1.60 \times 10^{-5}$  cm<sup>2</sup> s<sup>−1</sup>.

example (the highest curve in Figure 16b); without considering the adsorption process, the theoretical current–time curve (○), matched to long times, is much lower than the experimental curve in the first 0.25 s. To fit the data in this initial period, the adsorption rate constant,  $k_{\text{ads}}$  (0.05 cm s<sup>−1</sup>), and  $N$  ( $9 \times 10^{-10}$  mol cm<sup>−2</sup>) were used. The experimental curves clearly indicate that there is an additional flux of  $\text{Ag}^+$  ions through the aqueous phase to the interface, which leads to a higher initial tip current. For the different potentials applied at the electrode in Figure 16b, the values of  $k_{\text{ads}}$  and  $N$  were all 0.05 cm s<sup>−1</sup> and  $9 \times 10^{-10}$  mol cm<sup>−2</sup>, providing confidence about this assignment. SECM experiments of  $\text{Ag}^+$  ion electrogeneration to observe solely the adsorption process, without DMFc in the DCE phase, gave  $i$ – $t$  curves which showed no evidence of  $\text{Ag}^+$  ion adsorption (see, for example, Figure 14). The fact that an electron donor is needed in the DCE phase to observe the short time phenomenon seen in the transients in Figure 16b suggests that the initial process could involve some electrodischarge or the interfacial association between  $\text{Ag}^+$  and DMFc. Note that if one considered purely a progressive nucleation process, the minimum in the chronoamperometric curve would be even more

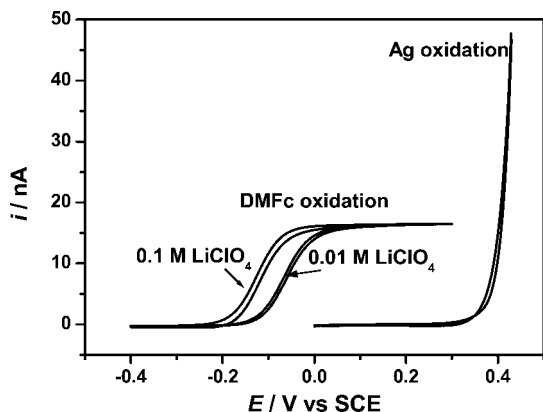


**Figure 18.** Cyclic voltammograms of Ag oxidation recorded at a 25  $\mu\text{m}$  diameter Ag UME in an aqueous solution containing 0.1 M  $\text{LiClO}_4$  and DMFc oxidation recorded at a 25  $\mu\text{m}$  diameter Pt UME in a DCE solution containing 5 mM DMFc and 0.1 M  $\text{TBAClO}_4$  with either 0.1 or 0.01 M  $\text{LiClO}_4$  in the aqueous phase. The scan rate was 20  $\text{mV s}^{-1}$ . An SCE in the aqueous phase served as the reference electrode.

pronounced than for the case of instantaneous nucleation shown. The experimental observations can only be accounted for by a relatively high initial flux to the interface, coupled with the nucleation and growth process.

#### 4.2.3. Effect of Concentration of Organic Reductant DMFc.

Figure 17a summarizes current–time transients recorded at the Ag UME with three different concentrations of DMFc in DCE. As the concentration of DMFc decreases, the position of the peak maximum in the current transient appears at longer times and its magnitude becomes smaller. This is perhaps counterintuitive, because one might consider that depletion of DMFc should occur sooner at lower concentration. However, the reaction rate depends on particle size and the higher the DMFc concentration, the quicker the particles grow. Thus, the higher the DMFc concentration, the earlier the depletion of DMFc. Figure 17b shows the best match of theory to experiment for the initial part of the transients. The best fit parameters were  $k = 5 \text{ cm s}^{-1}$  ( $L = 7.0 \times 10^{-5} \text{ cm}$ ),  $k = 7 \text{ cm s}^{-1}$  ( $L = 8.0 \times 10^{-5} \text{ cm}$ ), and  $k = 10 \text{ cm s}^{-1}$  ( $L = 8.0 \times 10^{-5} \text{ cm}$ ) for DMFc concentrations of 0.01, 0.02, and 0.03 M, respectively. Thus, the rate constant is strongly dependent on the DMFc concentration.

**4.2.4. Effect of Reaction Driving Force.** In this system, the reaction driving force ( $\chi$ ) is determined by the difference in the formal potentials of the  $\text{Ag}/\text{Ag}^+$  (w) and  $\text{DMFc}/\text{DMFc}^+$  (o) couples ( $\Delta E^0 = E_{\text{Ag}^+/\text{Ag}}^0 - E_{\text{DMFc}^+/\text{DMFc}}^0$ ) and the Galvani potential drop across the ITIES ( $\Delta_\phi^w$ ):

$$\chi = \Delta E^0 + \Delta_\phi^w \quad (36)$$

In this case,  $\Delta_\phi^w$  was controlled by the partitioning of a single potential-determining ion,  $\text{ClO}_4^-$ , in the two phases. To consider briefly the effect of driving force across the L/L interface, two different concentrations of the aqueous supporting electrolyte,  $\text{LiClO}_4$ , were studied, while the concentration of the supporting electrolyte in the DCE phase,  $\text{TBAClO}_4$ , was maintained constant.

At standard temperature and pressure, assuming experimental conditions where the activity coefficients of  $\text{ClO}_4^-$  in water and

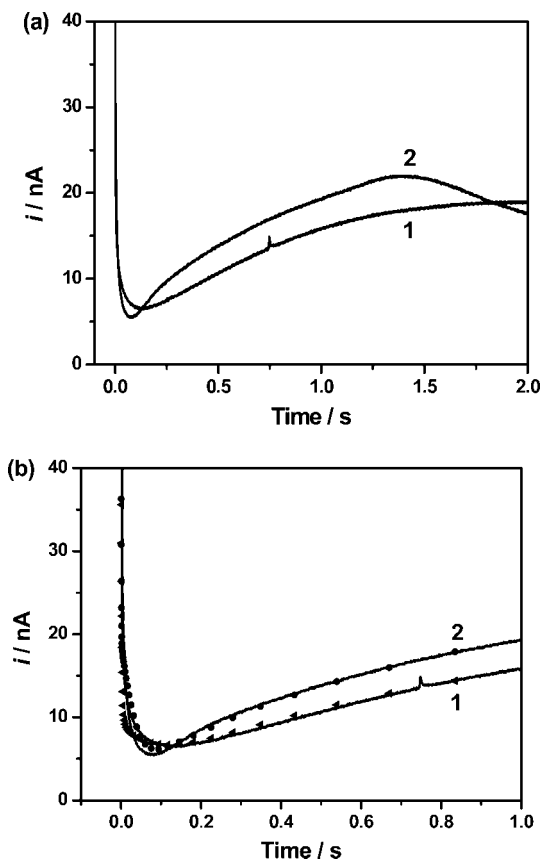


**Figure 19.** (a) Current–time transients recorded at a 25  $\mu\text{m}$  diameter Ag UME with different concentrations of  $\text{LiClO}_4$  in the aqueous phase. The aqueous solutions contained 0.01 M  $\text{LiClO}_4$  and 0.09 M  $\text{KNO}_3$  (curve 1) and 0.1 M  $\text{LiClO}_4$  (curve 2), while the DCE solution contained 0.03 M DMFc and 0.1 M  $\text{TBAClO}_4$  in each case. The tip–interface separations were 3.0  $\mu\text{m}$  (curve 1) and 3.4  $\mu\text{m}$  (curve 2). The UME potential was stepped from 0 to 0.39 V (vs SCE). (b) Simulations of experimental tip currents (solid symbols) over a time scale of 1.0 s. The parameters providing the best fit between the experimental and simulated curves were ( $\blacktriangle$ )  $k = 5 \text{ cm s}^{-1}$  ( $d = 3.0 \mu\text{m}$ ) and ( $\bullet$ )  $k = 10 \text{ cm s}^{-1}$  ( $d = 3.4 \mu\text{m}$ ). Other parameters used for simulation were  $c^* = 1.0 \text{ mM}$ ,  $L = 8.0 \times 10^{-5} \text{ cm}$ ,  $k_{\text{ads}} = 0.05 \text{ cm s}^{-1}$ ,  $N = 9 \times 10^{-10} \text{ mol cm}^{-2}$ , and  $D_{\text{Ag}^+} = 1.60 \times 10^{-5} \text{ cm}^2 \text{ s}^{-1}$ .

DCE are constant, within the concentration range of interest, the following equation should hold for  $\Delta_\phi^w$

$$\Delta_\phi^w = \Delta_\phi^{w0'} - 0.059 \log \frac{[\text{ClO}_4^-]_o}{[\text{ClO}_4^-]_w} \quad (37)$$

where w and o denote the water and organic (DCE) phases,  $[\text{ClO}_4^-]_w$  and  $[\text{ClO}_4^-]_o$  are the concentrations of  $\text{ClO}_4^-$  in water and the DCE phase, respectively, and  $\Delta_\phi^{w0'}$  is the formal transfer potential for  $\text{ClO}_4^-$  ( $\Delta_\phi^{w0'} = -0.17 \text{ V}$  (vs standard hydrogen electrode, SHE)).<sup>45</sup> Thus, the ratio of the  $\text{ClO}_4^-$  concentrations in the two phases determines the Galvani potential drop across the L/L interface. We point out that as the formal transfer potential of  $\text{Ag}^+$  ions from water to DCE,  $\Delta_\phi^{w0'}$ , has been reported as 0.50 V (vs SHE),<sup>46</sup> the possible transfer of  $\text{Ag}^+$  ions from water to DCE can be excluded in the interfacial Galvani potential difference range of this system.

Cyclic voltammograms of the anodic oxidation of Ag in the aqueous solution and DMFc oxidation in the DCE solution with 0.1 and 0.01 M  $\text{LiClO}_4$  in the aqueous phase, respectively, are shown in Figure 18. It can be seen that the driving force for the reduction of  $\text{Ag}^+$  by DMFc is greater by approximately 60 mV with 0.1 M  $\text{LiClO}_4$ .



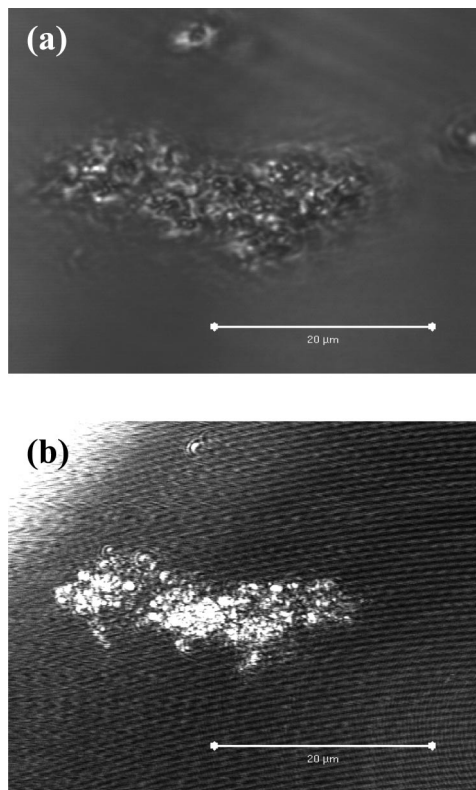


**Figure 20.** Visualization by confocal microscopy in transmission (a) and reflection modes (b) of Ag particles formed at a water/DCE interface. The scale bar is 20  $\mu\text{m}$ . See the text for SECM parameters used to form the particles.

Figure 19a shows typical current–time curves recorded at the Ag UME with the two different concentrations of  $\text{LiClO}_4$  in the aqueous phase. The transient with 0.1 M  $\text{LiClO}_4$  shows a sharper minimum and more steeply rising portion thereafter. The tip current increases more slowly for the case of 0.01 M  $\text{LiClO}_4$ , which is because the reaction driving force is smaller with a lower concentration of  $\text{ClO}_4^-$  in the aqueous phase. Clearly, the smaller driving force leads to a slower growth rate as manifested in a more gradual increase of the tip current with time. By fitting the experimental curves to the numerical simulation (Figure 19b), the rate constant,  $k$ , was 5  $\text{cm s}^{-1}$  (0.01 M  $\text{LiClO}_4$ ) and 10  $\text{cm s}^{-1}$  (0.1 M  $\text{LiClO}_4$ ). In both cases,  $L = 8 \times 10^{-5}$  cm best described the data. These preliminary data suggest that the Galvani potential difference has a rather weak effect on the nucleation and growth process. This contrasts with many simpler ET processes at L/L interfaces, which show much stronger potential-dependent rate constants.<sup>47</sup>

**4.3. Microscopy of Ag Particles Formed at the Water/DCE Interface.** CLSM was employed to confirm that particles were formed at the interface. For these experiments, the SECM potential-step experiments lasted for 5 s. The applied UME potential was 0.39 V and the tip to interface separation was 3.5  $\mu\text{m}$ . This ensured there would be sufficient deposition for optical characterization. After the potential step, the interface formed at the small hole inside the cell was examined by CLSM in both transmission and reflection modes, using a dipping lens. Typical confocal microscopy images obtained using the two modes are shown in Figure 20. In both modes, Ag deposits were visible as dark/bright particles. The patch of particles is irregular because the cell had to be moved from an electrochemistry environment to the confocal microscope, which took a few minutes and involved the cell being carried some distance. Nonetheless, one can clearly see that an area approximating to

the UME size is observed. This is consistent with the simulations presented earlier. Some agglomeration of particles is observed, which again highlights why the quantitative analysis of transients focused on short times, where this problem was less likely.

## 5. Conclusions

The SECM-induced deposition of Ag particles at a nonpolarizable water/DCE interface by the electron transfer reaction between aqueous electrogenerated  $\text{Ag}^+$  ions and DCE-phase DMFc has been demonstrated. Using a two-electrode system, with an Ag UME as the source of  $\text{Ag}^+$  ions, factors influencing the interfacial deposition process, such as the tip–interface separation, the potential applied at the tip, the concentration of the reductant in the DCE phase, and the L/L interfacial reaction driving force, have been investigated by SECM potential-step chronoamperometry. A theoretical model was developed that allowed the rate constants for Ag particle growth at the water/DCE interface to be obtained, along with an estimate of the particle density. Key observations were that the apparent particle density increased with an increasing flux of electrogenerated  $\text{Ag}^+$  ions and that the initial nucleation process was coupled to an adsorption process. Furthermore, the rate of Ag particle growth showed only a weak dependence on the Galvani potential across the L/L interface.

This study has demonstrated that SECM is a promising technique to study interfacial metal nucleation and growth processes quantitatively and the methodology could readily be used to study solid/liquid interfaces and extended to other materials and composites. The methodology is particularly sensitive to coupled processes, such as adsorption phenomena, and could prove powerful in the study of phase formation at a wide variety of electrode/electrolyte interfaces. The type of approach described could also be expanded to include the electrogeneration of other metal ions from solid electrodes and amalgams (e.g., mercury) and liquid filled micro- and nanopipets.

**Acknowledgment.** This research was funded by the Dorothy Hodgkin Postgraduate Awards Scheme (F.L.) and the EPSRC through the MOAC Doctoral Training Center (M.A.E.) and a project grant to support J.G. We appreciate the help and advice of Anna L. Whitworth, particularly with the confocal microscopy measurements.

## References and Notes

- (1) Binder, W. H. *Angew. Chem., Int. Ed.* **2005**, *44*, 5172.
- (2) Dryfe, R. A. W. *Phys. Chem. Chem. Phys.* **2006**, *8*, 1869.
- (3) Cheng, Y. F.; Schiffrin, D. J. *J. Chem. Soc. Farad. Trans.* **1996**, *92*, 3865.
- (4) (a) Johans, C. J.; Lahtinen, R.; Kontturi, K.; Schiffrin, D. J. *J. Electroanal. Chem.* **2000**, *488*, 99. (b) Johans, C.; Kontturi, K.; Schiffrin, D. J. *J. Electroanal. Chem.* **2002**, *526*, 29.
- (5) (a) Platt, M.; Dryfe, R. A. W.; Robert, E. P. L. *Chem. Commun.* **2002**, 2324. (b) Platt, M.; Dryfe, R. A. W.; Roberts, E. P. L. *Electrochim. Acta* **2003**, *48*, 3037. (c) Platt, M.; Dryfe, R. A. W.; Roberts, E. P. L. *Electrochim. Acta* **2004**, *49*, 3937. (d) Platt, M.; Dryfe, R. A. W. *Phys. Chem. Chem. Phys.* **2005**, *7*, 1807. (e) Platt, M.; Dryfe, R. A. W. *J. Electroanal. Chem.* **2007**, *599*, 323.
- (6) Dryfe, R. A. W.; Simm, A. O.; Kralj, B. *J. Am. Chem. Soc.* **2003**, *125*, 13014.
- (7) Guo, J. D.; Tokimoto, T.; Othman, R.; Unwin, P. R. *Electrochem. Commun.* **2003**, *5*, 1005.
- (8) (a) Trojanek, A.; Langmaier, J.; Samec, Z. *Electrochem. Commun.* **2006**, *8*, 475. (b) Trojanek, A.; Langmaier, J.; Samec, Z. *J. Electroanal. Chem.* **2007**, *599*, 160.
- (9) Lahtinen, R. M.; Fermin, D. J.; Jensen, H.; Kontturi, K.; Girault, H. H. *Electrochem. Commun.* **2000**, *2*, 230.
- (10) (a) Johans, C.; Clohesy, J.; Fantini, S.; Kontturi, K.; Cunnane, V. J. *Electrochem. Commun.* **2002**, *4*, 227. (b) Johans, C.; Liljeroth, P.; Kontturi, K. *Phys. Chem. Chem. Phys.* **2002**, *4*, 1067. (c) Scholz, F.; Hasse, U. *Electrochem. Commun.* **2005**, *7*, 541. (d) Lepkova, K.; Clohesy, J.;

Cunnane, V. J. *Electrochim. Acta* **2008**, *53*, 6273. (e) Knake, R.; Fahmi, A. W.; Tofail, S. A. M.; Clohessy, J.; Mihov, M.; Cunnane, V. J. *Langmuir* **2005**, *21*, 1001.

(11) (a) Rao, C. N. R.; Kulkarni, G. U.; Thomas, P. J.; Agrawal, V. V.; Saravanan, P. J. *Phys. Chem. B* **2003**, *107*, 7391. (b) Rao, C. N. R.; Kulkarni, G. U.; Agrawal, V. V.; Gautum, U. K.; Ghosh, M.; Tumkurkar, U. J. *Colloid Interface Sci.* **2005**, *289*, 305.

(12) (a) Yogeve, D.; Efrima, S. J. *Phys. Chem.* **1988**, *92*, 5754. (b) Yogeve, D.; Deutsch, M.; S.; Efrima, S. J. *Phys. Chem.* **1989**, *93*, 4147. (c) Yogeve, D.; Shtutina, S.; Efrima, S. J. *Phys. Chem.* **1990**, *94*, 752. (d) Zeiri, L.; Younes, O.; Efrima, S.; Deutsch, M. J. *Phys. Chem. B* **1997**, *101*, 9299. (e) Schwartz, H.; Harel, Y.; Efrima, S. *Langmuir* **2001**, *17*, 3884.

(13) Reincke, F.; Hickey, S. G.; Kegel, W. K.; Vanmaekelbergh, D. V. *Angew. Chem., Int. Ed.* **2004**, *43*, 458.

(14) Sakata, J. K.; Dwoskin, A. D.; Vigorita, J. L.; Spain, E. M. J. *Phys. Chem. B* **2005**, *109*, 138.

(15) Greef, R.; Peat, R.; Peter, L. M.; Pletcher, D.; Robinson, J. *Instrumental Methods in Electrochemistry*; Ellis Horwood: Chichester, 1985; pp 283–316.

(16) (a) Crooks, R. M.; Zhao, M. Q.; Sun, L.; Chechik, V.; Yeung, L. K. *Acc. Chem. Res.* **2001**, *4*, 181. (b) Song, Y.; Murray, R. W. J. *Am. Chem. Soc.* **2002**, *124*, 7096. (c) Hicks, J. F.; Miles, D. T.; Murray, R. W. J. *Am. Chem. Soc.* **2002**, *124*, 13322. (d) Peng, Z. Q.; Wang, E. K.; Dong, S. J. *Electrochem. Commun.* **2002**, *4*, 210. (e) Cheng, W. L.; Dong, S. J.; Wang, E. K. *Electrochem. Commun.* **2002**, *4*, 412. (f) Quinn, B. M.; Liljeroth, P.; Kontturi, K. J. *Am. Chem. Soc.* **2002**, *124*, 12915.

(17) Bonnemann, H.; Richards, R. M. *Eur. J. Inorg. Chem.* **2001**, 2455.

(18) Kanie, O.; Grotenbreg, G.; Wong, C. *Angew. Chem., Int. Ed.* **2000**, *39*, 4545.

(19) Ma, Z.; Sui, S. *Angew. Chem., Int. Ed.* **2002**, *41*, 2176.

(20) Alivisatos, A. P.; Johnson, K. P.; Peng, X.; Wilson, T. E.; Loweth, C. J.; Burchez, M. P.; Schultz, P. G., Jr. *Nature* **1996**, *382*, 609.

(21) Faraday, M. *Philos. Trans. R. Soc. London* **1857**, *147*, 145.

(22) Guainazzi, G.; Silvestri, G.; Serravalle, G. J. *Chem. Soc., Chem. Commun.* **1975**, 200.

(23) Bard, A. J.; Fan, R. F.; Kwak, J.; Lev, O. *Anal. Chem.* **1989**, *61*, 132.

(24) James, P. I.; Garfias-Mesais, L. F.; Moyer, P. J.; Smyrl, W. H. J. *Electrochem. Soc.* **1998**, *145*, L64.

(25) (a) Gonsalves, M.; Barker, A. L.; Macpherson, J. V.; Unwin, P. R.; O'Hare, D.; Winlove, C. P. *Biophys. J.* **2000**, *78*, 1578. (b) Gonsalves, M.; Macpherson, J. V.; O'Hare, D.; Winlove, C. P.; Unwin, P. R. *Biochim. Biophys. Acta* **2000**, *66*, 1524. (c) Macpherson, J. V.; Unwin, P. R. *Anal. Chem.* **2000**, *72*, 276. (d) Macpherson, J. V.; Unwin, P. R. *Anal. Chem.* **2001**, *73*, 550. (e) Fonseca, S. M.; Barker, A. L.; Ahmed, S.; Kemp, T. J.; Unwin, P. R. *Chem. Commun.* **2003**, 1002. (f) Fonseca, S. M.; Barker, A. L.; Ahmed, S.; Kemp, T. J.; Unwin, P. R. *Phys. Chem. Chem. Phys.* **2004**, *6*, 5218.

(26) (a) Craston, D. H.; Lin, C. W.; Bard, A. J. J. *Electrochem. Soc.* **1988**, *135*, 785. (b) Husser, O. E.; Craston, D. H.; Bard, A. J. J. *Electrochem. Soc.* **1989**, *136*, 3222. (c) Bard, A. J.; Denuault, G.; Lee, C.; Mandler, D.;

Wipf, D. O. *Acc. Chem. Res.* **1990**, *23*, 357. (d) Mandler, D.; Bard, A. J. J. *Electrochem. Soc.* **1989**, *136*, 3143. (e) Mandler, D.; Bard, A. J. J. *Electrochem. Soc.* **1990**, *137*, 1079. (f) Mandler, D.; Bard, A. J. J. *Electrochem. Soc.* **1990**, *137*, 2468.

(27) Yatziv, Y.; Turyan, I.; Mandler, D. J. *Am. Chem. Soc.* **2002**, *124*, 5618.

(28) Turyan, I.; Etienne, M.; Mandler, D.; Schuhmann, W. *Electroanalysis* **2005**, *17*, 538.

(29) Day, T. M.; Unwin, P. R.; Macpherson, J. V. *Nano Lett.* **2007**, *7*, 51.

(30) Burt, D. P.; Cervera, J.; Mandler, D.; Macpherson, J. V.; Manzanares, J. A.; Unwin, P. R. *Phys. Chem. Chem. Phys.* **2005**, *7*, 2955.

(31) Martin, R. D.; Unwin, P. R. J. *Chem. Soc., Faraday Trans.* **1998**, *94*, 753.

(32) Barker, A. L.; Macpherson, J. V.; Slevin, C. J.; Unwin, P. R. J. *Phys. Chem. B* **1998**, *102*, 1586.

(33) Hills, G. J.; Schiffrin, D. J.; Thompson, J. *Electrochim. Acta* **1974**, *19*, 657.

(34) Scharifker, B.; Hills, G. *Electrochim. Acta* **1983**, *28*, 879.

(35) Sluyters-Rehbach, M.; Wijenberg, J. H. O. J.; Bosco, E.; Sluyters, J. H. J. *Electroanal. Chem.* **1987**, *236*, 1.

(36) Mirkin, M. V.; Nilov, A. P. J. *Electroanal. Chem.* **1990**, *283*, 35.

(37) Heerman, L.; Tarallo, A. J. *Electroanal. Chem.* **1999**, *470*, 70.

(38) Trojánek, A.; Langmaier, J.; Samec, Z. J. *Electroanal. Chem.* **2007**, *599*, 160.

(39) Heyrovsky, J.; Kuta, J. *Instrumental Techniques in Electrochemistry*; Academic Press, New York, 1966.

(40) Johans, C.; Kontturi, K.; Schiffrin, D. J. J. *Electroanal. Chem.* **2002**, *526*, 29.

(41) *CRC Handbook of Chemistry and Physics*, 86th ed.; CRC Press: Boca Raton, FL, 2005.

(42) Unwin, P. R.; Bard, A. J. J. *Phys. Chem.* **1992**, *96*, 5035.

(43) (a) Macpherson, J. V.; Unwin, P. R. J. *Phys. Chem.* **1995**, *99*, 14824.

(b) Macpherson, J. V.; Unwin, P. R. J. *Phys. Chem.* **1995**, *99*, 3338. (c) Macpherson, J. V.; Unwin, P. R. J. *Phys. Chem.* **1994**, *98*, 1704.

(44) Unwin, P. R.; Macpherson, J. V.; Martin, R. D.; McConville, C. F. *Proc. Electrochem. Soc.* **2000**, *99–28*, 104–121.

(45) Hundhammer, B.; Solomon, T. J. *Electroanal. Chem.* **1983**, *157*, 19.

(46) Reymond, F.; Laguer, G.; Carrupt, P.; Girault, H. H. J. *Electroanal. Chem.* **1998**, *451*, 59.

(47) (a) Tsionsky, M.; Bard, A. J.; Mirkin, M. V. J. *Phys. Chem.* **1996**, *100*, 17881. (b) Barker, A. L.; Unwin, P. R.; Amemiya, S.; Zhou, J. F.; Bard, A. J. J. *Phys. Chem. B* **1999**, *103*, 7260. (c) Ding, Z. F.; Quinn, B. M.; Bard, A. J. J. *Phys. Chem. B* **2001**, *105*, 6367. (d) Zhang, J.; Barker, A. L.; Unwin, P. R. J. *Electroanal. Chem.* **2000**, *483*, 95. (e) Zhang, Z. Q.; Yuan, Y.; Sun, P.; Su, B.; Guo, J. D.; Shao, Y. H.; Girault, H. H. J. *Phys. Chem. B* **2002**, *106*, 6713. (f) Barker, A. L.; Unwin, P. R.; Zhang, J. *Electrochem. Commun.* **2001**, *3*, 372.

JP809165T